BIOCHEMISTRY

Design of a minimal di-nickel hydrogenase peptide

Jennifer Timm[1,2]†, Douglas H. Pike[2]†‡, Joshua A. Mancini[1,2]†, Alexei M. Tyryshkin[1,2]†, Saroj Poudel[1,2]†, Jan A. Siess[2], Paul M. Molinaro[3], James J. McCann[3], Kate M. Waldie[4], Ronald L. Koder[3], Paul G. Falkowski[1]*, Vikas Nanda[2]*

Ancestral metabolic processes involve the reversible oxidation of molecular hydrogen by hydrogenase. Extant hydrogenase enzymes are complex, comprising hundreds of amino acids and multiple cofactors. We designed a 13–amino acid nickel-binding peptide capable of robustly producing molecular hydrogen from protons under a wide variety of conditions. The peptide forms a di-nickel cluster structurally analogous to a Ni-Fe cluster in [NiFe] hydrogenase and the Ni-Ni cluster in acetyl-CoA synthase, two ancient, extant proteins central to metabolism. These experimental results demonstrate that modern enzymes, despite their enormous complexity, likely evolved from simple peptide precursors on early Earth.

INTRODUCTION

In the contemporary world, molecular hydrogen (H_2) is only used as a source of energy by specialized microorganisms in anaerobic environments, but early in Earth's history, the first microbial metabolisms were almost certainly dependent on H_2 (*1*, *2*). Reversible biological oxidation of H_2 is catalyzed by hydrogenases, redox metalloenzymes with iron-iron (Fe-Fe), nickel-iron (NiFe), or iron-only (Fe) active sites (*3*, *4*). Extant hydrogenases are complex nanomachines that comprise hundreds of amino acids, multiple subunits, and multiple metal cofactors that ferry electrons to the active Ni-Fe site (*3*). Phylogenetic studies suggest that [NiFe] hydrogenases are ancestral (*4*); soluble nickel and iron ions were far more abundant under anoxic conditions that characterized the Archean and Proterozoic oceans than today (*5*, *6*). However, the first hydrogenases must have been much smaller and simpler. Model studies of a Ni-substituted rubredoxin suggest that a small protein can evolve H_2 (*7*). Here, we demonstrate that a very short peptide can readily form dinuclear Ni-Ni clusters capable of catalytically evolving H_2. Such peptides are simple enough that they could have emerged spontaneously during a prebiotic stage in the origin of life, giving rise to the first metabolic reaction networks.

RESULTS

Computational peptide design

In extant [NiFe] hydrogenases, active-site metal ions are coordinated by four cysteines, cyanide (CN^-), carbon monoxide (CO), and water (Fig. 1, left). The cysteines are separated by hundreds of amino acids, making it challenging to design a short peptide analog directly from the native sequence. Instead, we surveyed minimal metal-binding sites in existing protein structures for geometries compatible with Ni^{2+} ion coordination within a short, continuous region of sequence (fig. S1). Replacing carboxylates with thiols in an existing calcium-binding site (*8*), we identified a CxCGCxxxxxCG pattern. The variable (x) positions were chosen computationally using the structure-guided protein design platform protCAD (*9*), resulting in the initial designs (see Materials and Methods for details). However, as described below, nickel binding titrations indicated a 2:1 metal:peptide stoichiometry, motivating us to model a dinuclear site within the same scaffold. In the final nickelback (NB) model (Fig. 1, middle), metal coordination mimics the features of the acetyl-CoA (coenzyme A) synthase (ACS) di-nickel A-cluster site (Fig. 1, right). As in native ACS, a CGC motif provides two backbone amides (G4 and C5) and two side-chain thiols (C3 and C5) to coordinate the (distal) Ni^{2+} ion coordination in a square-planar geometry. The C3 and C5 thiols also serve as bridging ligands to a second (proximal) Ni^{2+} ion whose coordination is completed with the remaining cysteines C1 and C12. We define proximal/distal Ni^{2+} sites based on nomenclature from equivalent positions of nickel ions in ACS A-cluster and hydrogenase. Coordinates for the density functional theory (DFT)–optimized model of NB-2Ni are provided on ModelArchive (fig. S2) (*10*).

Synthesis and nickel reconstitution

Apo-NB was produced by 9-fluorenyl methoxycarbonyl solid-phase synthesis and reconstituted with Ni^{2+} salts at 50°C. The di-nickel cluster assembly was monitored by ultraviolet-visible absorption and circular dichroism (CD) spectroscopies (Fig. 2, A and C). Two optically active species were identified: an intermediate stage (2NB-1Ni) with the 2:1 (peptide:Ni) stoichiometry and the active stage (NB-2Ni) saturating at 1:2 stoichiometry. Isosbestic points in the CD spectra (marked with arrows in Fig. 2A) indicate a direct conversion from 2NB-1Ni to NB-2Ni during the reconstitution. Spectral decomposition of the CD spectra with a two-component model (figs. S5 and S6) was used to determine fractional concentrations of 2NB-1Ni and NB-2Ni during the course of the Ni reconstitution (Fig. 2B). To allow quantitative estimation of peptide concentrations, a tryptophan-containing NB variant (NB-Trp, N8W) was also examined (figs. S7, S12, and S14).

[1]Environmental Biophysics and Molecular Ecology Program, Department of Marine and Coastal Sciences and Department of Earth and Planetary Sciences, Rutgers University, New Brunswick, NJ 08901, USA. [2]Center for Advanced Biotechnology and Medicine and the Department of Biochemistry and Molecular Biology, Robert Wood Johnson Medical School, Rutgers University, Piscataway, NJ 08854, USA. [3]Department of Physics, The City College of New York, New York, NY 10016, USA. [4]Department of Chemistry and Chemical Biology, Rutgers University, Piscataway, NJ 08854, USA.
†These authors contributed equally to this work.
‡Present address: Quantum-Si, Guilford, CT, USA.
*Corresponding author. Email: falko@marine.rutgers.edu (P.G.F.); vik.nanda@rutgers.edu (V.N.)

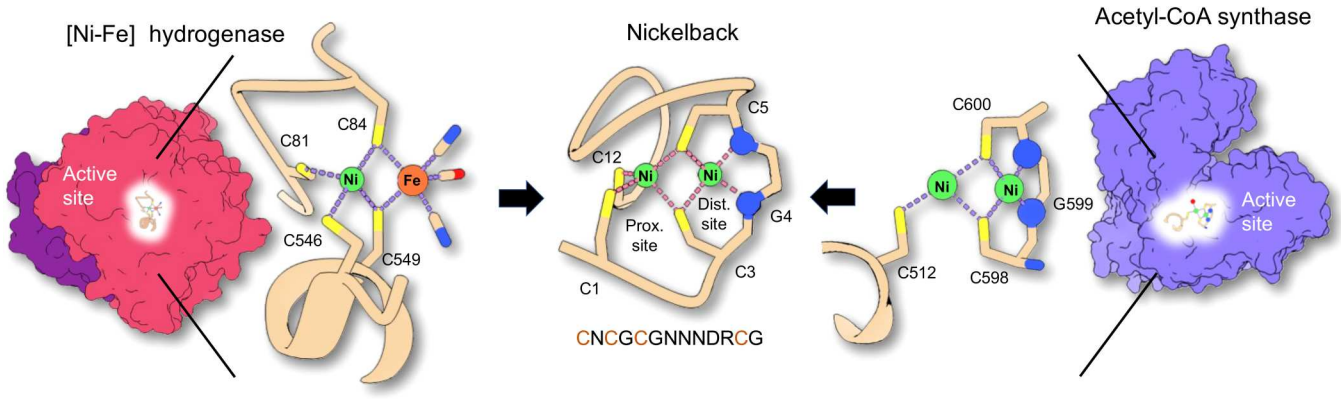

Fig. 1. Model structure of NB and comparison to natural enzymes. [Ni-Fe] hydrogenase (left) (PDB ID: 5XLE) and ACS (right) (PDB ID: 1RU3) are large, complex proteins with active di-metal sites coordinated by a few ligands. The model structure of NB (middle) combines elements of both active sites in a 13-residue polypeptide.

Structural and chemical stability

Dynamic light scattering (DLS) measurements of NB-2Ni showed a dominant monodisperse species with a radius of hydration consistent with a compact monomeric peptide (fig. S20). The fully reconstituted NB-2Ni was confirmed to be stable at pH 5.5 to 10 (fig. S8), in a wide temperature range from 20° to 90°C (fig. S9), showing no sign of aggregation when stored in solutions for several months, and even in the presence of molecular oxygen or dissolved bicarbonate (figs. S10 and S11). In an ancient-Earth context, NB-2Ni would be expected to be stable over a range of predicted ocean pH values and temperatures that early peptide catalysts would encounter during the Archean Eon (*11*).

The enhanced stability of NB-2Ni likely originates from its compact, closed-shell chelating geometry (Fig. 1), where the CNCGC segment provides a tight tetradentate coordination for both Ni^{2+} ions. There are no other cysteine ligands that potentially could cross-link and lead to oligomerization. The closed-shell chelation geometry of NB discriminates it from other examined Cys-containing polypeptides, many of which oligomerize in the presence of Ni^{2+} and other divalent metal ions (*12*, *13*).

Redox activity

In parallel with optical studies, we probed the redox activity of both the intermediate 2NB-1Ni and the mature NB-2Ni complexes using cyclic voltammetry (CV; Fig. 2D and figs. S16 to S18). The 2NB-Ni species showed no redox activity. The S-shaped reduction wave developed only at high concentrations of reconstituted Ni^{2+} (Fig. 2D), with the catalytic current at −850 mV [versus standard hydrogen electrode (SHE)] directly correlated with the fraction of NB-2Ni species (Fig. 2E). This redox potential is more than sufficient to drive hydrogen evolution reaction (HER), with E_0 = −440 mV at pH 7.5.

Cysteine-nickel controls

Control studies on free cysteine complexed with metal showed that while nickel chelates are formed, they have a very different coordination structure compared to NB-2Ni as measured by CD (fig. S19A). Cysteine-Ni chelates did not form monodisperse species as measured by DLS (fig. S20). CV confirmed that cysteine-Ni chelates did not exhibit a catalytic current consistent with the reductive evolution of hydrogen. Together, these observations are consistent with NB-2Ni forming a stable, unique coordination complex capable of redox chemistry that cannot be attributed to nonspecific metal-thiol complexes or chelates in cysteine-rich peptides (*12*–*14*).

Photocatalysis

Catalytic H_2 production by NB-2Ni was demonstrated using a photochemical assay with an organic dye (EosinY) as a photosensitizer and triethanolamine (TEOA) as a sacrificial electron donor irradiated at 540 nm (*15*). H_2 evolution was quantified using gas chromatography. At pH 8, the turnover number TON = 500 and the turnover frequency TOF = 0.2 H_2/min were derived (Fig. 2F). Despite the small size of NB, its TOF is comparable to that of other Ni-binding designs (0.1 to 0.9 H_2/min), while the TON is larger (*16*, *17*).

EPR structural characterization of the reduced state

We probed the structure of the di-nickel site in NB-2Ni by electron paramagnetic resonance (EPR). As both nickels are in the 2+ oxidation state, the resting state of NB-2Ni is not EPR active. Addition of the strong reductant europium diethylenetriamine pentaacetic acid [Eu(II)DTPA, E_0 = −1.1 V at pH 8; (*18*)] failed to produce any detectable concentration of one-electron reduced NB-2Ni, likely due to fast catalytic HER turnover with all reductant being consumed on a time scale of seconds and before the sample could be frozen. However, it was possible to trap a one-electron reduced NB-2Ni at a sufficiently high yield of 10 to 25% when Eu(II)DTPA was added in the presence of small ligands, either CN^- or bicarbonate, and after increasing the pH to 8 to 10 (Fig. 3A and fig. S21). A detectable yield (10%) of one-electron reduced NB-2Ni was also obtained with deuterium oxide (D_2O) without small ligands (fig. S22). The EPR signal was identical in all cases, indicating that small ligands or solvent deuteration merely slowed down the reduction turnover, thus trapping substantial fractions in a one-electron reduced state.

EPR of the reduced state (Fig. 3A) was characteristic of a d^9 electron configuration with Ni^{1+} in distorted octahedral, square-pyramidal, or square-planar coordination and with the unpaired electron preferentially residing on a d_{x2-y2} orbital (*19*, *20*). Both nickel sites in NB-2Ni have this coordination symmetry in our model structures (fig. S2). However, a distal-site Ni^{1+} can be excluded because backbone amides would appear as strong hyperfine

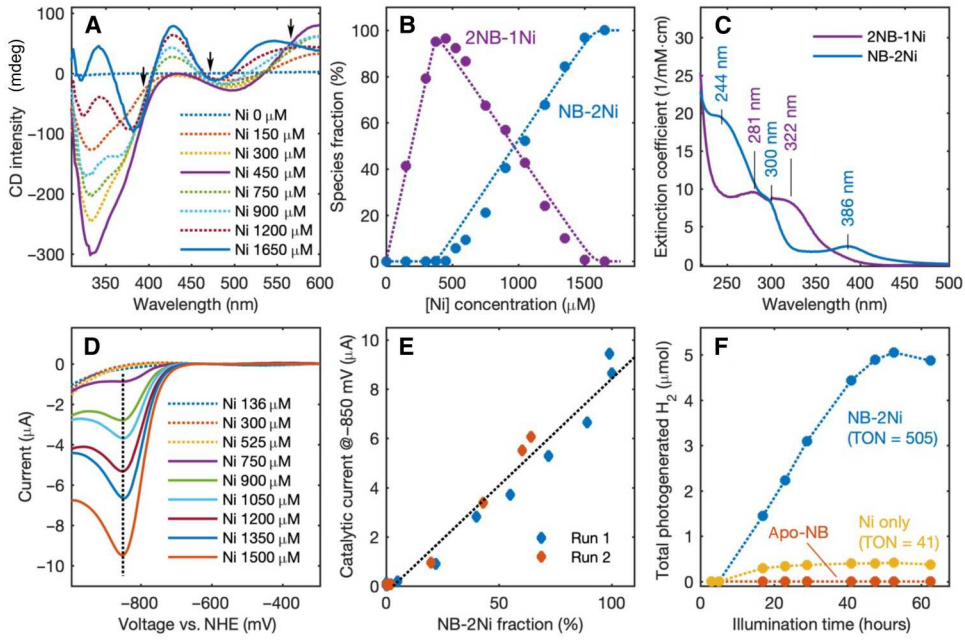

Fig. 2. Assembly and activity of NB. (**A**) CD spectra of NB as a function of added Ni: [NB] = 750 μM (pH 7.5), temperature = 50°C. The peak at 340 nm (assigned to 2NB-1Ni) at first grows, reaching the maximum at [Ni] = 450 μM (solid purple line), and then declines at even higher [Ni] concentrations. The peak at 430 nm (assigned to NB-2Ni) starts to develop only at [Ni] > 500 μM, and it grows monotonously to saturate around [Ni] = 1650 μM (solid blue line). Black arrows show isosbestic points. (**B**) Fractional concentrations of 2NB-1Ni and NB-2Ni as extracted from the two-component spectral decomposition of the CD spectra from (A), as demonstrated in figs. S5 and S6. The dashed lines are the fits using a two-step reconstitution model: apo-NB → 2NB-1Ni → NB-2Ni (fig. S6). The upper bounds for Ni^{2+} binding constants were estimated from the fit to be around 1 μM in both 2NB-1Ni and NB-2Ni. Replications of this titration confirmed metal saturation beyond a 1:2 peptide-nickel stoichiometry (fig. S7). (**C**) Absorption spectra of pure 2NB-1Ni and NB-2Ni with characteristic bands labeled. (**D**) Reduction waves in bulk solution CV experiments at different stages of Ni reconstitution in NB: [NB] = 750 μM (pH 7.5), added [Ni] is indicated for each trace (full traces in figs. S14 to S16). NHE - normal hydrogen electrode. The catalytic current at −850 mV (vertical dashed line) starts to develop only at [Ni] > 500 μM, and it grows linearly with the NB-2Ni fraction as demonstrated in (**E**). (**F**) Photochemical H_2 evolution by NB-2Ni (10 μM) with EosinY (500 μM) and TEOA (500 mM), 540-nm illumination (pH 8) at 37°C.

interactions, which were not observed (figs. S21, S22, and S25 to S29). The reduced Ni^{1+} most likely occupies the proximal site (Fig. 3C). Similar Ni^{1+} EPR signatures have been reported for [NiFe] hydrogenase (*21*) and the ACS proximal site (*22*), supporting the structural homology of NB-2Ni to these two enzymes. The *g*-factor rhombicity, g = (2.27, 2.08, 2.05), in the reduced NB-2Ni is comparable with g = (2.26 to 2.3, 2.11 to 2.12, and 2.05) detected in the one-electron reduced "Ni-L" state of [NiFe] hydrogenase, obtained by low-temperature photolysis of the H_2-reduced enzyme (*21*, *23*). One of the cysteine residues at the proximal Ni^{1+} site in Ni-L was predicted to be protonated (*24*). Our electron spin echo envelope modulation (ESEEM)/hyperfine sublevel correlation (HYSCORE) experiments resolved one exchangeable proton at a distance of 2.5 Å from the proximal Ni^{1+} in NB-2Ni that is consistent with the predicted distance to a protonated cysteine (figs. S25, S26, S28, and S29). In addition, three-pulse ESEEM spectra of the reduced NB-2Ni identified one nitrogen atom at a distance of 3.1 Å that was tentatively assigned to a nearby backbone amide based on nuclear quadrupolar coupling parameters (figs. S27 and S30). While the presence of small ligands such as CN^- or bicarbonate was critically important for trapping detectable concentrations of the one-electron reduced NB-2Ni, all measured EPR characteristics, including the *g*-factor values as well as the hyperfine/quadrupolar couplings of the exchangeable proton and the amide nitrogen, were unaffected despite the nature of the coordinating ligands (figs. S21 to S29). These results strongly suggest that small ligands were not involved in direct coordination of the proximal Ni^{1+} site, and instead, they interact at the remote (distal) Ni^{2+} site. Consistent with this conclusion, our EPR/ESEEM experiments did not reveal any detectable transitions from ^{14}N of CN^- or from ^{13}C of bicarbonate that would be expected if they coordinated directly with the proximal Ni^{1+} site (figs. S21, S22, and S27).

EPR structural characterization of the oxidized state

Conversely, oxidation of NB-2Ni with iridium chloride generated a Ni^{3+} EPR spectrum characteristic of a d^7 electron configuration with an unpaired electron residing on a d_{z2} orbital (*19*, *20*) and with a *g*-factor symmetry consistent with square-planar or elongated octahedral coordination (Fig. 3B). Both the shape and the *g*-factor values of the oxidized NB-2Ni signal are very similar to those of oxidized nickel superoxide dismutase (Ni-SOD), where Ni^{3+} is in a square-pyramidal coordination with two backbone amides, two cysteines, and a histidine in the axial position (*25*). While NB does not contain histidine, the addition of 10 mM imidazole to oxidized NB-2Ni (Fig. 3B, red trace) recapitulated the ^{14}N hyperfine splitting seen in Ni-SOD, now resolved on the $g_{||}$ = 2.014 peak. This supports a Ni^{3+} at the distal position in the oxidized state (Fig. 3C).

On the basis of these assignments for nickel oxidation states, we would expect that removing C1 and C12 might eliminate the proximal site while retaining the distal one. We designed NBΔP with C1 and C12 replaced by serine. Nickel titrations of NBΔP saturated at a

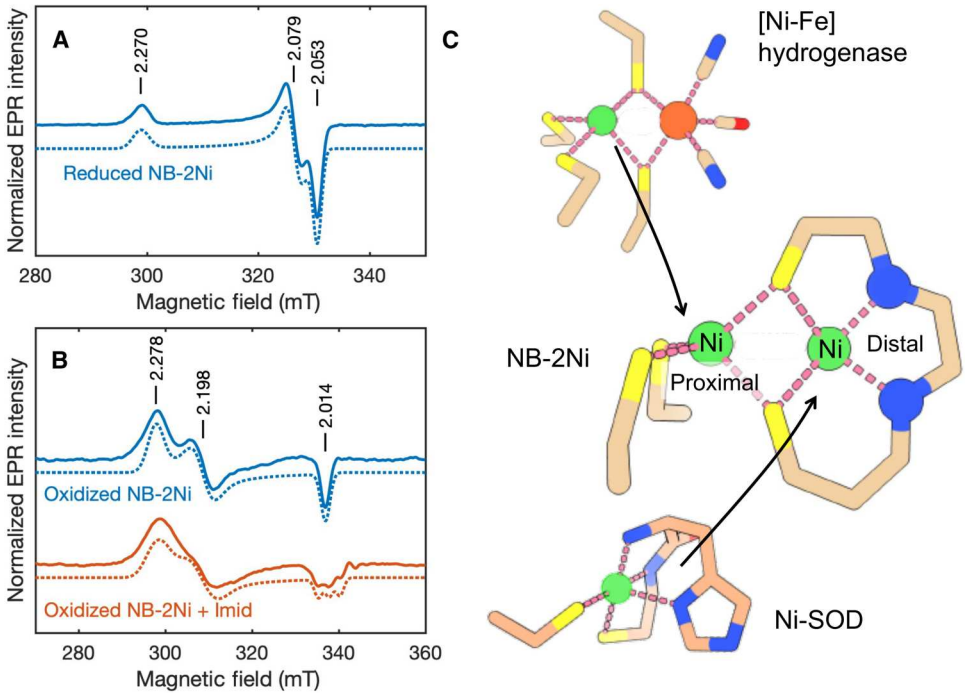

Fig. 3. Structural characterization of NB-2Ni. EPR spectra of (**A**) reduced and (**B**) oxidized NB-2Ni at pH 10, measured at 20 and 30 K, respectively: solid lines, experiment; dashed lines, EPR simulations. The principal *g*-factor values are marked with vertical lines and numbers. The oxidized NB-2Ni in (B) was measured in the absence (blue traces) and presence (red traces) of imidazole ligands (10 mM). (**C**) The *g*-factor symmetry of reduced (oxidized) NB-2Ni is similar to Ni^{1+} in [NiFe] hydrogenase and Ni^{3+} in Ni-SOD where Ni ions are found in distinctly different coordination sites, e.g., Ni^{1+} and Ni^{3+}, respectively. Both these Ni sites are represented in di-nickel NB-2Ni.

1:1 complex, with a distinct CD spectrum compared to NB-2Ni (fig. S12). EPR of oxidized NBΔP-Ni is comparable with oxidized NB-2Ni (fig. S23), confirming the assignment of Ni^{3+} at the distal site. On the other hand, trapping a one-electron reduced form of NBΔP-Ni with Eu(II)DTPA in the presence or absence of small ligands or in deuterated solvent was not successful. No catalytic wave was observed for NBΔP-Ni in CV (fig. S18), indicating that the distal Ni alone is insufficient for HER catalysis. Furthermore, no catalytic wave was observed for free cysteine complexes with Ni^{2+} (fig. S19B).

DISCUSSION

In general, hydrogen reduction catalysis involves a sequence of two 1-electron reduction steps and two protonation steps ($2H^+ + 2e^- \rightarrow H_2$). The NB-2Ni voltammograms resolved only one reduction wave (Fig. 2D), implying that the two steps involved one-electron reduction reactions with overlapping redox potentials. This result suggests that the reaction may proceed through a CECEC mechanism where the two sequential one-electron reduction steps (E) are functionally separated by one protonation step (C) (*7*, *26*). The proposed CECEC mechanism is consistent with pH titration experiments where NB-2Ni, in its resting state, is protonated at pH below 9 (fig. S32). While the exact nature of the protonated NB-2Ni state is unknown, on the basis of its apparent pK_a = 9.1, we propose the protonation of a cysteine residue directly coordinated at a proximal Ni^{2+} site in NB-2Ni. This protonation of proximal cysteine in the resting NB-2Ni state may be essential for promoting the reaction, as well as for tuning the reduction potential of proximal Ni^{2+} down to less negative values, effectively reducing the overpotential requirements. The protonation of thiolate groups proximal to a Ni^{2+} center had been widely discussed as important intermediates in a hydrogen reduction cycle for both small-molecule complexes and protein-derived systems, including the Ni-L state in [NiFe] hydrogenase (*7*, *17*, *23*, *27*).

Studies on Ni-substituted rubredoxin have shown robust H_2 evolution with an apparent TON between 32 and 100, depending on protein concentrations and a TOF of ~0.5 min^{-1} (*7*). While these numbers are similar to the ones obtained with NB-2Ni, with our complex showing a higher TON, differences in assay conditions complicate making direct comparisons. These and other examples highlight the potential of nickel enzymes to have played a central role in ancient hydrogen metabolism (*28*).

The kinetic catalytic parameters of NB-2Ni are sufficient to function as the electron sink in a metabolic half-cell, where evolution and diffusion of hydrogen gas could maintain a redox disequilibrium. Assuming a peptide concentration of 10 nM, just a few molecules per cell, lower than hydrogenase abundances in modern organisms (*29*), NB-2Ni could maintain a steady H_2 concentration of >20 nM (see the Supplementary Materials for calculation). For comparison, active iron reducers in marine sediments have been observed at ~1 nM [H_2] (*30*, *31*). An NB-like peptide could have plausibly served as an electron sink in early metabolic pathways. Notably, we have not observed hydrogen oxidation in this system. To drive metabolisms such as methanogenesis/acetogenesis, H_2-oxidizing catalysts would have to have been present.

Simple, metal-binding peptides capable of redox reactions almost certainly were an essential step in the origins of life (*24*, *32*). Moreover, these peptides are likely generalists, capable of

catalyzing many reactions (*33*). Given the similarity to the A-cluster site of ACS, it is tempting to hypothesize that NB may be able to reduce carbon species. We anticipate that exploring the catalytic potential of NB and similar metallopeptides beyond H_2 could elucidate the peptide origins of many of the key ancient metabolic reaction networks (*1*, *34*, *35*).

Engineering candidate peptide catalysts has led to the unexpected observation that extremely short amino acid sequences can exhibit substantial stability and activity. Similar to NB-2Ni, the designed 12–amino acid protein, ambidoxin, complexed a 4Fe-4S cluster with four cysteines and was capable of hundreds of reversible redox cycles (*36*). Ambidoxin was designed to mimic the active site of bacterial ferredoxins, natural protein electron carriers that were fivefold larger. These two metallopeptides point to a general approach for engineering catalysts by structural analysis of large metalloenzyme active sites. The chemical stability and functional potential of small peptides complexed with transition metals make them plausible ancestors in the evolution of oxidoreductases and challenge the long-held idea that early enzymes may have been poor catalysts that required optimization of activity by extensive molecular evolution (*33*, *37*, *38*).

MATERIALS AND METHODS

Design strategy

The [Ni-Fe] hydrogenase dinuclear site is coordinated by four cysteines separated by several hundred residues in sequence. Toward the goal of developing a minimalist peptide catalyst, we examined metal coordination sites in natural proteins where ligands were much closer together. On the basis of previous nickel-based hydrogen-evolving catalysts (*7*), we began by designing a mononuclear nickel site.

The initial scaffold was based on the high-resolution structure of a Mn^{2+}-binding site at the C terminus of parvalbumin (*39*). A manganese ion was octahedrally coordinated by four side-chain carboxylates, three of which were close in sequence, with the DxDxD motif adopting tight turns around the metal (fig. S1A). In this case, the metal was fully coordinated, with an additional backbone carbonyl oxygen and water. Given that Ni^{2+} is frequently octahedral in proteins (*40*), we examined whether a derived site replacing carboxylates with thiols would appropriately bind nickel.

Starting from the parvalbumin structure, residues 90 to 102, D90, D92, D94, and E102 were replaced with cysteine, setting side-chain rotamers to optimally coordinate the nickel ion. Using the protEvolver tool in the molecular modeling platform protCAD, the sequence of the remaining nonligand amino acids was chosen. protCAD is a molecular modeling platform that allows torsional sampling of the backbone and side-chain degrees of freedom as well as sequence substitutions. Scoring is based on a force field that combines the AMBER ff14SB nonbonding terms (*41*), the Dunbrack bbdep rotamer library (*42*), and implicit solvation (*9*). protEvolver uses a genetic algorithm implementation to rapidly sample sequence space and can be scaled to run in parallel on a number of compute nodes. protCAD and the protEvolver code are open source and available for download; see Data and materials availability.

Several thousand structural models were generated. The top-ranked among these were subjected to extended molecular dynamics simulations using AMBER (*43*). Models were solvated in an 8-Å water layer, using the TIP3P water model (*44*) and the ff14SB force field (*41*). The system was minimized in steepest descent, followed by conjugate gradient minimization. Parameters for nickel were chosen to favor tetrahedral coordination with a S-Ni bond length of 2.27 Å. Periodic boundaries were set under constant volume, and the system was thermalized from 0 to 300 K using Langevin dynamics and a collision frequency of 3 ps^{-1}. Molecular dynamics simulations were run for 3.0 μs at 300 K. Calculations were performed with a 2-fs time step. Structural sampling produced a distorted square-planar nickel coordination geometry despite the setting of tetrahedral constraints. This indicated that there were limitations to the modeling assumptions and the use of molecular mechanics to explore the metallopeptide structure.

Dinuclear models and DFT calculations

Observation of a second nickel binding necessitated additional metal ligands beyond the four cysteine thiols. In [Ni-Fe] hydrogenase, additional coordination of the iron was provided by cyanide and carbon monoxide, which were not explicitly incorporated as a part of metal reconstitution. Instead, the di-nickel site of ACS [Protein Data Bank (PDB) ID: 1MJG] and single nickel ions in Ni-SOD (PDB ID: 1T6U) and the [Ni-Fe] hydrogenase accessory protein, HypB, by backbone amides, led us to examine backbone amide nitrogens as potential metal ligands.

Two plausible models were examined, one where the distal nickel is coordinated by cysteines C1 and C3, the "CNC" model (fig. S2), and one where the distal nickel is coordinated by cysteines C3 and C5, the "CGC" model (fig. S2). Models were constructed and sampled with molecular dynamics as described above (metal-ligand parameter files available; see Data and materials availability). We followed molecular mechanics optimization with DFT geometric optimization of both models.

CGC and CNC model geometry optimization calculations were performed using the ORCA quantum chemistry package (*45*). Initial rounds of calculations were undertaken with the use of the BP86 level of theory (*46*) using the Karlsruhe def2-SVP split valence polarization basis set applied to all atoms with the def2/J auxiliary basis set for Coulomb fitting and the Karlsruhe def2-TZVP triple-zeta polarization basis set applied to the nickel atoms (*47*). The split-RI-J approximation was used in the approximation of Coulomb integrals (*48*–*50*). Upon convergence of the initial round of calculations, a second round of calculations was undertaken on the final structure of CGC. The second optimization run used the segmented all-electron relativistically contracted (SARC) Karlsruhe def2-TZVP valence triple-zeta polarization basis set (*51*) with the fully decontracted def2/J (SARC/J) auxiliary basis set (*52*) for all atoms excluding nickel, which instead used the relativistically contracted Karlsruhe basis set ZORA-def2-TZVPP valence triple-zeta with two sets of polarization functions applied to nickel and the coordinating sulfurs. The RIJCOSX approximation (*53*), which incorporates the resolution of identity approximation (RI) and the chain-of-spheres approximation (COSX) for the formation of Coulomb and quantum mechanical exchange matrices, respectively, was used as well. Scalar relativistic all-electron effects were handled by using the zeroth-order regular approximation (ZORA) scalar relativistic Hamiltonian (*54*–*56*). A large and conservative grid size was chosen (DefGrid3 as per ORCAs syntax) along with a tight self-consistent field convergence threshold. Dispersion corrections were accounted for by using Grimme's DFT-D3(BJ) (*57*) atom-pairwise

dispersion correction with Becke-Johnson damping (*58*–*60*) and were used in both the initial and the second round of calculations. Aqueous solvation energies were calculated using the conductor-like polarizable continuum model (CPCM) (*61*) implemented in ORCA. A van der Waals–type cavity was used to treat electrostatic solvation effects within the Gaussian charge scheme (*62*). The water solvent had a dielectric constant of 80.4 set within the CPCM module.

The distal nickel site in both CGC and CNC models is square-planar (fig. S2). In CGC, the proximal nickel is in the square-pyramidal coordination with four equatorial ligands comprising three sulfurs (C1, C5, and C12), one backbone oxygen (R11), and one axial sulfur ligand (C3). The coordination geometry of the proximal nickel in CNC is distorted square-planar, which was coordinated by three sulfurs (C3, C5, and C12) and one nitrogen (C12). This is inconsistent with EPR measurements, leading us to eliminate the CNC model. Conversely, the coordination geometry of the proximal nickel in CGC was in concordance with EPR measurements. Although the CGC model is most consistent with EPR, we note that two α protons are close to the proximal nickel but were not observed by EPR, indicating that further model development is still necessary. CGC and CNC models of NB-2Ni are available in ModelArchive (*10*) under accession numbers ma-6lwmo, ma-3g061, and ma-iyjyy.

Peptide synthesis

For initial peptide screening, small quantities of peptides were synthesized using a microwave-assisted peptide synthesizer (Liberty Blue, CEM Corporations) as described before (*36*). In brief, the synthesis was carried out using standard solid-phase methods with diisopropylcarbodiimide (DIC) and ethyl (hydroxyimino) cyanoacetate (Oxyma) coupling agents in *N*,*N*′-dimethylformamide and subsequent purification with ether precipitation and reverse-phase high-pressure liquid chromatography using a C18 column and a H_2O/acetonitrile gradient with 0.1% trifluoroacetic acid in both solutions. The identity and purity of the peptides were confirmed using matrix-assisted laser desorption/ionization mass spectrometry analysis. Lyophilized peptide was stored at −20°C until used.

For detailed characterization, NB peptide was purchased from Genscript Biotech (Piscataway, NJ) as a lyophilized powder, which was stored frozen in aliquots until used. Peptides in this study were as follows: NB, CNCGCGNNNDRCG; NB-Trp, CNCGCGNWNDRCG (N8W); NBΔP, SNCGCGNNNDRSG (removal of the proximal site, C1S/C12S).

Nickel reconstitution and titrations

Lyophilized apo-NB peptides were dissolved in a buffer containing 25 mM Hepes, 100 mM NaCl, and 3.75 mM freshly prepared TCEP (tris-2-carboxyethyl-phosphine hydrochloride), with pH adjusted to 7.5 to 9.2, to give a final peptide concentration of 0.75 to 1.0 mM. The apo-NB solution was deoxygenized by purging with 100% nitrogen gas for at least 20 min inside an airtight glass vial. Nickel reconstitution was done in an airtight 1-cm quartz optical cuvette sealed with a septum screw cap. The cuvette was placed inside the sample compartment of a CD spectrometer (AVIV 420) with the spectrometer thermostat set at 50°C. The progress in nickel reconstitution to NB peptides was directly monitored through the CD measurements. Varying amounts of Ni^{2+} from an oxygen-free $NiCl_2$ stock solution were added using a purged Hamilton syringe.

For regular nickel reconstitution, the $NiCl_2$ concentration corresponding to 2 molar equivalents of NB peptides was added in one shot, mixed by inversion of the cuvette multiple times, and incubated at 50°C for at least 2 hours or overnight. The reconstitution at room temperature was also successful but took substantially longer times of up to 48 hours. The progress in Ni reconstitution to peptides was monitored by periodically measuring CD spectra between 300 and 600 nm, and the reconstitution was considered to be complete when the CD spectra stopped changing anymore by further incubation.

For the nickel titration experiment, small (substoichiometric) aliquots of $NiCl_2$ were added to the peptide solutions, and the completion of each reconstitution step was monitored by CD spectrometry before the addition of more $NiCl_2$. The titration was considered complete when further addition of $NiCl_2$ did not result in any changes in the CD spectra. In addition to CD experiments, CV measurements were carried out on the same reconstitution solution at selected nickel concentration steps as described below.

pH titrations

To investigate the effect of pH on nickel coordination in NB-2Ni and on electrochemical potential, the sample buffer was modified to contain 10 mM N-Cyclohexyl-2-aminoethanesulfonic acid (CHES), 10 mM potassium phosphate, 10 mM MES, and 10 mM Hepes, with 100 mM NaCl and 3.75 mM TCEP. The pH at each step was adjusted using NaOH/HCl, with the solution purged with nitrogen after each adjustment. CD spectroscopy was used to monitor pH-dependent changes in the NB-2Ni coordination, and circular voltammetry was used for redox titrations.

Conversion of dynode voltage to absorption

The dynode voltage in the CD spectrometer can be converted into the absorption using the following equation: $\text{Abs} = 7.344 \times \log_{10}(\text{DV1}/\text{DV0})$, with 7.344 as the dynode gain (specific to our CD spectrometer), DV1 as the dynode voltage measured as a function of wavelength for the desired sample, and DV0 as the dynode voltage measured using the same settings for the blank (baseline) sample.

L-cysteine controls

To investigate the behavior of nonspecific nickel coordination, L-cysteine was reconstituted in parallel to NB peptide using equivalent conditions: 50 mM Hepes (pH 7.5), 100 mM NaCl, and 5 mM TCEP. NB (750 μM; containing four cysteines in the sequence) or 3 mM L-cysteine was dissolved in the buffer and deoxygenized by purging with 100% nitrogen gas for at least 20 min inside an airtight glass vial. $NiCl_2$ (1.5 mM) was added to each of the samples to facilitate an equivalent ratio of four cysteines to two Ni^{2+} in both. Reconstitutions were incubated at room temperature for 2 days (48 hours) and monitored by CD. Their electrochemical properties were investigated using circular voltammetry.

Dynamic light scattering

DLS experiments were carried out on a Zetasizer (v7.13, Malvern Panalytical Ltd.) in airtight, nitrogen-purged quartz cuvettes using the manufacturer′s standard operating protocols for size determination of standard protein. Buffer, L-cysteine plus $NiCl_2$

(4Cys-2Ni), and NB-2Ni were measured and analyzed using Zetasizer software v7.13.

EPR sample preparation

All sample preparations were carried out in an anaerobic chamber (CoyLabs vinyl chamber), containing a nitrogen (95%)/hydrogen (5%) gas mixture. To obtain reduced NB-2Ni complexes, 100 μl of the 2Ni-reconstituted peptides at a concentration of 750 μM was preincubated with 5 to 50 mM sodium bicarbonate or 5 mM $K_4Fe(CN)_6$ for 20 min at room temperature and then mixed with an equal volume of a buffer containing 100 mM CHES (pH 9.8) or Hepes (pH 7.5) and 50% (v/v) glycerol, before sequential addition of 1.5 mM $Eu(II)Cl_2$ (2 molar equivalents with respect to NB-2Ni) and 1.5 mM DTPA (*18*). The reduced NB-2Ni peptides in deuterated D_2O buffers were prepared similarly, with the exception that no bicarbonate or cyanide ligands were added, and using a partially deuterated d_3-glycerol. Oxidized NB-2Ni peptides were made following a similar procedure with the exception of adding a 10 to 50 mM $Na_2IrCl_6{\cdot}6H_2O$ oxidant during the last step.

The final concentration of the NB-2Ni peptides in all EPR samples was 375 μM. After mixing, the samples were immediately transferred to 4-mm OD quartz EPR tubes and then sealed with rubber caps before taking them from the anaerobic chamber and instantly freezing in liquid nitrogen (about 30 s between mixing and freezing). The frozen samples were flame-sealed and stored at liquid nitrogen until the experiments.

EPR spectroscopy

All EPR experiments were performed with a Bruker EPR spectrometer (Elexsys580e) operating at X-band microwave frequency. Helium-flow cryostats (Oxford ESR900 and CF935) equipped with an Oxford temperature controller (ITC503) were used for cryogenic temperatures.

Continuous-wave EPR experiments were done at a temperature of 20 K for the reduced NB-Ni^{1+} centers and at 30 K for the oxidized NB-Ni^{3+} centers. The following experimental settings were used: microwave frequency, 9.496 GHz; microwave power, 200 μW (reduced NB-Ni^{1+}) and 2 mW (oxidized NB-Ni^{3+}); modulation amplitude, 1 to 2 mT. Concentration yields of the reduced NB-Ni^{1+} or oxidized NB-Ni^{3+} centers in each sample were determined by comparing the integrated intensities of the measured $Ni^{1+/3+}$ signals against the EPR standard with a known number of spins (a $CuSO_4{\cdot}5H_2O$ crystal of known weight in a mineral oil).

Pulsed EPR experiments, including two-pulse ESEEM (π/2-τ-π-τ-echo), three-pulse ESEEM (π/2-τ-π/2-T-π/2-τ-echo), four-pulse HYSCORE (π/2-τ-π/2-t_1-π-t_2-π/2-τ-echo), and Davies electron nuclear double resonance (see below) (*63*–*66*), were performed to characterize the nuclear spin environment of reduced/oxidized $Ni^{1+/3+}$ centers. Phase cycling was used as required in each pulsed experiment to eliminate contributions from unwanted echoes (*63*).

Before Fourier transformation (FT), the ESEEM/HYSCORE time domains were baseline-corrected by fitting the oscillating decays with stretched exponential decay functions, then dividing the experimental decay by the fit function, and lastly subtracting a unity. This baseline correction procedure resulted in FT ESEEM spectral intensities that were automatically normalized to a unit echo signal amplitude. This normalization procedure allowed us to directly compare spectral amplitudes in ESEEM spectra measured for different samples with different $Ni^{1+/3+}$ concentrations, etc. (*64*).

After FT, linear phase correction was applied to the FT spectra to correct for missing dead times. In the case of two-pulse ESEEM, the dead time (t_0) was determined by an initial τ delay between the π/2 and π pulses in the experiment. In the case of three-pulse ESEEM, the correction time was calculated as ($\tau + t_0$), where τ is the fixed delay between the first π/2 and second π/2 pulses in the three-pulse sequence, and t_0 is the initial delay between the second and third pulses. In the case of HYSCORE, the linear phase correction was applied in both directions with the correction time calculated as ($\tau/2 + t_0$) (*67*), where t_0 is the initial delay between the second and third pulses or the third and fourth pulses. All ESEEM/HYSCORE spectra presented in this work are shown as normalized and phase-corrected cosine Fourier transforms.

Other experimental pulsed EPR settings were as follows: microwave frequency, 9.776 GHz; magnetic fields, 309 mT (the $g_{||}$ field orientation) and 336 mT (the $g_{\perp}$ field orientation) for reduced NB-Ni^{1+} centers and 345 mT ($g_{||}$) and 309 to 318 mT ($g_{\perp}$) for oxidized NB-Ni^{3+} centers; microwave π/2 and π pulses, 16 and 32 ns, respectively; initial τ delay, 104 ns (two-pulse ESEEM) and 40 ns (three-pulse ESEEM/HYSCORE); integration window, 16 ns (ESEEM/HYSCORE) and 60 ns (field-sweep echo-detected EPR); shot repetition times, 1 to 2 ms; and temperature, 20 to 30 K. All EPR/ESEEM simulations were performed using the EasySpin toolbox for MATLAB (www.easyspin.org/) (*68*).

Electrochemistry

All electrochemical experiments were carried out in an anaerobic atmosphere continuously purging nitrogen gas though the solution and headspace of the electrochemical cell. The CV experiments were set up using a Bio-Logic potentiostat (EC50) and a three-electrode configuration with a Ag/AgCl electrode (BASi) as a reference and a platinum wire as a counter electrode. A glassy carbon electrode (3 mm, MF-2012, BASi) was used as a working electrode, and it was polished with (1 μM) alumina slurry before every measurement. For every experiment, 5 ml of NB-Ni peptide at various concentrations was filled into a three-port Echem cell and connected to the electrodes while purging the solution with N_2. During the CV scan, the purging needle was withdrawn from the solution while still purging the headspace. Data were acquired using the EC-lab software (V10.44) and then baseline-corrected and analyzed using MATLAB. All potentials quoted in this work were referenced to an SHE and calculated as $E(\text{SHE}) = E(\text{Ag/AgCl}) + 205$ mV.

Photochemical experiments

Photocatalytic activity of Ni-reconstituted NB peptides toward H_2 evolution was examined in the presence of EosinY dye (−910 mV versus SHE) as a photosensitizer and TEOA as a sacrificial electron donor (*15*). The samples [10 μM NB, 500 μM EosinY, and 200–500 mM TEOA in Hepes buffer (pH 8.0), with 100 mM NaCl] of a typical volume of 1 ml were placed in airtight 13.5-ml glass vials sealed with a 10-mm-thick rubber stopper. Before illumination, the samples were purged with nitrogen gas for at least 20 min to remove any traces of oxygen.

The samples were placed into the box lined with aluminum foil from inside and were illuminated with green light (540 nm) from two 5-W light-emitting diode bulbs installed in the microscope light source (fig. S3). The incident light intensity on the samples

of ~0.2 mW/cm^2 was measured using an Ophir photodiode power meter (Nova II with PD300-3W-V1). During the course of the photochemical reaction, the amount of H_2 gas produced in the headspace of the vials was probed periodically using a gas chromatographer (SRI Instruments, Model 310) equipped with a thermal conductivity detector and using nitrogen as a carrier gas.

Supplementary Materials

This PDF file includes:

Figs. S1 to S32
References

REFERENCES AND NOTES

1. P. G. Falkowski, T. Fenchel, E. F. Delong, The microbial engines that drive Earth's biogeochemical cycles. *Science* **320**, 1034–1039 (2008).
2. K. H. Nealson, F. Inagaki, K. Takai, Hydrogen-driven subsurface lithoautotrophic microbial ecosystems (SLiMEs): Do they exist and why should we care? *Trends Microbiol.* **13**, 405–410 (2005).
3. W. Lubitz, H. Ogata, O. Rüdiger, E. Reijerse, Hydrogenases. *Chem. Rev.* **114**, 4081–4148 (2014).
4. J. W. Peters, G. J. Schut, E. S. Boyd, D. W. Mulder, E. M. Shepard, J. B. Broderick, P. W. King, M. W. W. Adams, [FeFe]- and [NiFe]-hydrogenase diversity, mechanism, and maturation. *Biochim. Biophys. Acta Molec. Cell Res.* **1853**, 1350–1369 (2015).
5. H. Liu, K. O. Konhauser, L. J. Robbins, W.-d. Sun, Global continental volcanism controlled the evolution of the oceanic nickel reservoir. *Earth Planet. Sci. Lett.* **572**, 117116 (2021).
6. R. J. P. Williams, The bakerian lecture, 1981 natural selection of the chemical elements. *Proc. Royal Soc. Lond. B Biol. Sci.* **213**, 361–397 (1981).
7. J. W. Slater, S. C. Marguet, H. A. Monaco, H. S. Shafaat, Going beyond structure: Nickel-substituted rubredoxin as a mechanistic model for the [NiFe] hydrogenases. *J. Am. Chem. Soc.* **140**, 10250–10262 (2018).
8. O. Gutten, L. Rulíšek, How simple is too simple? Computational perspective on importance of second-shell environment for metal-ion selectivity. *Phys. Chem. Chem. Phys.* **17**, 14393–14404 (2015).
9. D. H. Pike, V. Nanda, Empirical estimation of local dielectric constants: Toward atomistic design of collagen mimetic peptides. *Biopolymers* **104**, 360–370 (2015).
10. Computational Structural Biology Group at the SIB Swiss Institute of Bioinformatics at the Biozentrum (University of Basel), vol. 2022; modelarchive.org/.
11. J. Krissansen-Totton, G. N. Arney, D. C. Catling, Constraining the climate and ocean pH of the early Earth with a geological carbon cycle model. *Proc. Natl. Acad. Sci. U.S.A.* **115**, 4105–4110 (2018).
12. H. Kozlowski, B. Decock-Le Révérend, D. Ficheux, C. Loucheux, I. Sovago, Nickel(II) complexes with sulfhydryl containing peptides. Potentiometric and spectroscopic studies. *J. Inorg. Biochem.* **29**, 187–197 (1987).
13. T. Kowalik-Jankowska, H. Kozlowski, E. Farkas, I. Sóvágó, Nickel ion complexes of amino acids and peptides, in *Nickel and Its Surprising Impact in Nature*, A. Sigel, H. Sigel, R. K. O. Sigel, Eds. (Wiley, 2007), vol. 2, pp. 63–107.
14. K. Krzywoszyńska, J. Swiątek-Kozłowska, S. Potocki, M. Ostrowska, H. Kozłowski, Triplet of cysteines—Coordinational riddle? *J. Inorg. Biochem.* **204**, 110957 (2020).
15. A. Bachmeier, F. Armstrong, Solar-driven proton and carbon dioxide reduction to fuels —Lessons from metalloenzymes. *Curr. Opin. Chem. Biol.* **25**, 141–151 (2015).
16. M. J. Stevenson, S. C. Marguet, C. R. Schneider, H. S. Shafaat, Light-driven hydrogen evolution by nickel-substituted rubredoxin. *ChemSusChem* **10**, 4424–4429 (2017).
17. D. Selvan, P. Prasad, E. R. Farquhar, Y. Shi, S. Crane, Y. Zhang, S. Chakraborty, Redesign of a copper storage protein into an artificial hydrogenase. *ACS Catalysis* **9**, 5847–5859 (2019).
18. K. A. Vincent, G. J. Tilley, N. C. Quammie, I. Streeter, B. K. Burgess, M. R. Cheesman, F. A. Armstrong, Instantaneous, stoichiometric generation of powerfully reducing states of protein active sites using Eu(II) and polyaminocarboxylate ligands. *Chem. Commun.* , 2590–2591 (2003).
19. M. V. Gastel, W. Lubitz, EPR investigation of [NiFe] hydrogenases, in *High Resolution EPR. Biological Magnetic Resonance*, L. Berliner, G. Hanson, Eds. (Springer, 2009), vol. 28, pp. 441–470.
20. A. Abragam, B. B. Bleaney, Electron paramagnetic resonance of transition ions. 277–345 (2012).
21. M. E. Pandelia, H. Ogata, L. J. Currell, M. Flores, W. Lubitz, Inhibition of the [NiFe] hydrogenase from *Desulfovibrio vulgaris* Miyazaki F by carbon monoxide: An FTIR and EPR spectroscopic study. *Biochim. Biophys. ActaBioenerg.* **1797**, 304–313 (2010).
22. G. Bender, T. A. Stich, L. Yan, R. D. Britt, S. P. Cramer, S. W. Ragsdale, Infrared and EPR spectroscopic characterization of a Ni(I) species formed by photolysis of a catalytically competent Ni(I)-CO Intermediate in the acetyl-CoA synthase reaction. *Biochemistry* **49**, 7516–7523 (2010).
23. M. van Gastel, W. Lubitz, EPR investigation of [NiFe] hydrogenases, in *High Resolution EPR–Biological Magnetic Resonance* (Springer, 2009), vol. 28, pp. 441–470. https://doi.org/10.1007/978-0-387-84856-3_10.
24. D. Rossetto, S. S. Mansy, Metals are integral to life as we know it. *Front. Cell Dev. Biol.* **10**, 864830 (2022).
25. D. P. Barondeau, C. J. Kassmann, C. K. Bruns, J. A. Tainer, E. D. Getzoff, Nickel superoxide dismutase structure and mechanism. *Biochemistry* **43**, 8038–8047 (2004).
26. A. Das, Z. Han, W. W. Brennessel, P. L. Holland, R. Eisenberg, Nickel complexes for robust light-driven and electrocatalytic hydrogen production from water. *ACS Catalysis* **5**, 1397–1406 (2015).
27. Z. Zhang, T. Yang, P. Qin, L. Dang, Nickel bis(dithiolene) complexes for electrocatalytic hydrogen evolution: A computational study. *J. Organomet. Chem.* **864**, 143–147 (2018).
28. M. Can, F. A. Armstrong, S. W. Ragsdale, Structure, function, and mechanism of the nickel metalloenzymes, CO dehydrogenase, and acetyl-CoA synthase. *Chem. Rev.* **114**, 4149–4174 (2014).
29. K. Gutekunst, D. Hoffmann, U. Westernströer, R. Schulz, D. Garbe-Schönberg, J. Appel, In-vivo turnover frequency of the cyanobacterial NiFe-hydrogenase during photohydrogen production outperforms in-vitro systems. *Sci. Rep.* **8**, 6083 (2018).
30. D. E. Canfield, E. Kristensen, B. Thamdrup, Thermodynamics and microbial metabolism. *Adv. Mar. Biol.* **48**, 65–94 (2005).
31. T. M. Hoehler, M. J. Alperin, D. B. Albert, C. S. Martens, Thermodynamic control on hydrogen concentrations in anoxic sediments. *Geochim. Cosmochim. Acta* **62**, 1745–1756 (1998).
32. F. Baymann, E. Lebrun, M. Brugna, B. Schoepp–Cothenet, M.-T. Giudici-Orticoni, W. Nitschke, The redox protein construction kit: Pre-last universal common ancestor evolution of energy-conserving enzymes. *Philos. Trans. R. Soc. Lond. B Biol. Sci.* **358**, 267–274 (2003).
33. R. A. Jensen, Enzyme recruitment in evolution of new function. *Annu. Rev. Microbiol.* **30**, 409–425 (1976).
34. N. Lane, J. F. Allen, W. Martin, How did LUCA make a living? Chemiosmosis in the origin of life. *BioEssays* **32**, 271–280 (2010).
35. D. E. Canfield, M. T. Rosing, C. Bjerrum, Early anaerobic metabolisms. *Philos. Trans. R. Soc. Biol. Sci.* **361**, 1819–1836 (2006).
36. J. D. Kim, D. H. Pike, A. M. Tyryshkin, G. V. T. Swapna, H. Raanan, G. T. Montelione, V. Nanda, P. G. Falkowski, Minimal heterochiral de novo designed 4Fe–4S binding peptide capable of robust electron transfer. *J. Am. Chem. Soc.* **140**, 11210–11213 (2018).
37. L. Giger, S. Caner, R. Obexer, P. Kast, D. Baker, N. Ban, D. Hilvert, Evolution of a designed retro-aldolase leads to complete active site remodeling. *Nat. Chem. Biol.* **9**, 494–498 (2013).
38. L. Jiang, E. A. Althoff, F. R. Clemente, L. Doyle, D. Röthlisberger, A. Zanghellini, J. L. Gallaher, J. L. Betker, F. Tanaka, C. F. Barbas III, D. Hilvert, K. N. Houk, B. L. Stoddard, D. Baker, De novo computational design of retro-aldol enzymes. *Science* **319**, 1387–1391 (2008).
39. J.-P. Declercq, B. Tinant, J. Parello, J. Rambaud, Ionic interactions with parvalbumins: Crystal structure determination of pike 4.10 parvalbumin in four different ionic environments. *J. Molec. Biol.* **220**, 1017–1039 (1991).
40. L. Rulísek, J. Vondrásek, Coordination geometries of selected transition metal ions (Co^{2+}, Ni^{2+}, Cu^{2+}, Zn^{2+}, Cd^{2+}, and Hg^{2+}) in metalloproteins. *J. Inorg. Biochem.* **71**, 115–127 (1998).
41. J. A. Maier, C. Martinez, K. Kasavajhala, L. Wickstrom, K. E. Hauser, C. Simmerling, ff14SB: Improving the accuracy of protein side chain and backbone parameters from ff99SB. *J. Chem. Theory Comput.* **11**, 3696–3713 (2015).
42. R. L. Dunbrack Jr., F. E. Cohen, Bayesian statistical analysis of protein side-chain rotamer preferences. *Protein Sci.* **6**, 1661–1681 (1997).
43. D. A. Case, H. M. Aktulga, K. Belfon, I. Y. Ben-Shalom, J. T. Berryman, S. R. Brozell, D. S. Cerutti, T. E. Cheatham III, G. A. Cisneros, V. W. D. Cruzeiro, T. A. Darden, R. E. Duke, G. Giambasu, M. K. Gilson, H. Gohlke, A. W. Goetz, R. Harris, S. Izadi, S. A. Izmailov, K. Kasavajhala, M. C. Kaymak, E. King, A. Kovalenko, T. Kurtzman, T. S. Lee, S. LeGrand, P. Li, C. Lin, J. Liu, T. Luchko, R. Luo, M. Machado, V. Man, M. Manathunga, K. M. Merz, Y. Miao, O. Mikhailovskii, G. Monard, H. Nguyen, K. A. O'Hearn, A. Onufriev, F. Pan, S. Pantano, R. Qi, A. Rahnamoun, D. R. Roe, A. Roitberg, C. Sagui, S. Schott-Verdugo, A. Shajan, J. Shen, C. L. Simmerling, N. R. Skrynnikov, J. Smith, J. Swails, R. C. Walker, J. Wang, J. Wang, H. Wei, R.M. Wolf, X. Wu, Y. Xiong, Y. Xue, D. M. York, S. Zhao, P. A. Kollman, Amber 2022, University of California, San Francisco (2022); https://ambermd.org/CiteAmber.php.

44. W. L. Jorgensen, Quantum and statistical mechanical studies of liquids. 10. Transferable intermolecular potential functions for water, alcohols, and ethers. Application to liquid water. *J. Am. Chem. Soc.* **103**, 335–340 (1981).
45. F. Neese, F. Wennmohs, U. Becker, C. Riplinger, The ORCA quantum chemistry program package. *J. Chem. Phys.* **152**, 224108 (2020).
46. A. D. Becke, Density-functional exchange-energy approximation with correct asymptotic behavior. *Phys. Rev. A. Gen. Phys.* **38**, 3098–3100 (1988).
47. F. Weigend, R. Ahlrichs, Balanced basis sets of split valence, triple zeta valence and quadruple zeta valence quality for H to Rn: Design and assessment of accuracy. *Phys. Chem. Chem. Phys.* **7**, 3297–3305 (2005).
48. J. L. Whitten, Coulombic potential energy intergrals and approximations. *J. Chem. Phys.* **58**, 4496 (1973).
49. B. I. Dunlap, J. Connolly, J. Sabin, On some approximations in applications of Xα theory. *J. Chem. Phys.* **71**, 3396 (1979).
50. F. Neese, An improvement of the resolution of the identity approximation for the formation of the Coulomb matrix. *J. Comput. Chem.* **24**, 1740–1747 (2003).
51. D. A. Pantazis, X. Y. Chen, C. R. Landis, F. Neese, All-electron scalar relativistic basis sets for third-row transition metal atoms. *J. Chem. Theory Comput.* **4**, 908–919 (2008).
52. F. Weigend, Accurate Coulomb-fitting basis sets for H to Rn. *Phys. Chem. Chem. Phys.* **8**, 1057–1065 (2006).
53. F. Neese, Prediction of molecular properties and molecular spectroscopy with density functional theory: From fundamental theory to exchange-coupling. *Coord. Chem. Rev.* **253**, 526–563 (2009).
54. E. van Lenthe, E.-J. Baerends, J. G. Snijders, Relativistic regular two-component Hamiltonians. *J. Chem. Phys.* **99**, 4597–4610 (1993).
55. E. van Lenthe, E.-J. Baerends, J. G. Snijders, Relativistic total energy using regular approximations. *J. Chem. Phys.* **101**, 9783–9792 (1994).
56. C. van Wüllen, Molecular density functional calculations in the regular relativistic approximation: Method, application to coinage metal diatomics, hydrides, fluorides and chlorides, and comparison with first-order relativistic calculations. *J. Chem. Phys.* **109**, 392–399 (1998).
57. S. Grimme, J. Antony, S. Ehrlich, H. Krieg, A consistent and accurate ab initio parametrization of density functional dispersion correction (DFT-D) for the 94 elements H-Pu. *J. Chem. Phys.* **132**, 154104 (2010).
58. A. D. Becke, E. R. Johnson, A density-functional model of the dispersion interaction. *J. Chem. Phys.* **123**, 154101 (2005).
59. E. R. Johnson, A. D. Becke, A post-Hartree-Fock model of intermolecular interactions. *J. Chem. Phys.* **123**, 024101 (2005).
60. E. R. Johnson, A. D. Becke, A post-Hartree-Fock model of intermolecular interactions: Inclusion of higher-order corrections. *J. Chem. Phys.* **124**, 174104 (2006).
61. V. Barone, M. Cossi, Quantum calculation of molecular energies and energy gradients in solution by a conductor solvent model. *Chem. A Eur. J.* **102**, 1995–2001 (1998).
62. M. Garcia-Ratés, F. Neese, Effect of the solute cavity on the solvation energy and its derivatives within the framework of the Gaussian charge scheme. *J. Comput. Chem.* **41**, 922–939 (2020).
63. A. Schweiger, G. Jeschke, *Principles of Pulse Electron Paramagnetic Resonance* (Oxford University Press, 2001).
64. S. A. Dikanov, Y. Tsvetkov, *Electron Spin Echo Envelope Modulation (ESEEM) Spectroscopy* (CRC Press, 1992).
65. P. Höfer, A. Grupp, H. Nebenführ, M. Mehring, Hyperfine sublevel correlation (hyscore) spectroscopy: A 2D ESR investigation of the squaric acid radical. *Chem. Phys. Lett.* **132**, 279–282 (1986).
66. E. Davies, A new pulse ENDOR technique. *Phys. Lett. A* **47**, 1–2 (1974).
67. A. Tyryshkin, S. Dikanov, D. Goldfarb, Sum combination harmonics in four-pulse ESEEM spectra. Study of the ligand geometry in aqua-vanadyl complexes in polycrystalline and glass matrices. *J. Magn. Reson. A* **105**, 271–283 (1993).
68. S. Stoll, Chapter 6—CW-EPR spectral simulations: Solid state, in *Methods in Enzymology—Electron Paramagnetic Resonance Investigations of Biological Systems by Using Spin Labels, Spin Probes, and Intrinsic Metal Ions, Part A* (Elsevier, 2015), vol. 563, pp. 121–142.
69. J. L. Wimmer, J. C. Xavier, A. D. N. Viera, D. P. H. Pereira, J. Leidner, F. L. Sousa, K. Kleinermanns, M. Preiner, W. F. Martin, Energy at origins: Favorable thermodynamics of biosynthetic reactions in the last universal common ancestor (LUCA). *Front. Microbiol.* **12**, 3903 (2021).
70. R. Conrad, W. Seiler, Methane and hydrogen in seawater (Atlantic Ocean). *Deep Sea Res. Part A. Oceanogr. Res. Pap.* **35**, 1903–1917 (1988).
71. C. N. Pace, F. Vajdos, L. Fee, G. Grimsley, T. Gray, How to measure and predict the molar absorption coefficient of a protein. *Protein Sci.* **4**, 2411–2423 (1995).
72. K. C. Ryan, A. I. Guce, O. E. Johnson, T. C. Brunold, D. E. Cabelli, S. C. Garman, M. J. Maroney, Nickel superoxide dismutase: Structural and functional roles of His1 and its H-bonding network. *Biochemistry* **54**, 1016–1027 (2015).
73. H.-I. Lee, J.-W. Lee, T.-C. Yang, S.-O. Kang, B. M. Hoffman, ENDOR and ESEEM investigation of the Ni-containing superoxide dismutase. *J. Biol. Inorg. Chem.* **15**, 175–182 (2010).
74. S. Dikanov, Y. D. Tsvetkov, M. Bowman, A. Astashkin, Parameters of quadrupole coupling of 14N nuclei in chlorophyll a cations determined by the electron spin echo method. *Chem. Phys. Lett.* **90**, 149–153 (1982).
75. H. L. Flanagan, D. J. Singel, Analysis of 14N ESEEM patterns of randomly oriented solids. *J. Chem. Phys.* **87**, 5606–5616 (1987).
76. S. Grimaldi, F. MacMillan, T. Ostermann, B. Ludwig, H. Michel, T. Prisner, $Q_H^{\bullet-}$ ubisemiquinone radical in the bo_3-type ubiquinol oxidase studied by pulsed electron paramagnetic resonance and hyperfine sublevel correlation spectroscopy. *Biochemistry* **40**, 1037–1043 (2001).
77. D. T. Edmonds, Nuclear quadrupole double resonance. *Phys. Rep.* **29**, 233–290 (1977).
78. K. Fukui, H. Ohya-Nishiguchi, H. Kamada, Electron spin echo envelope modulation study on oxovanadium (IV)-porphyrin complexes: Reinvestigation of hyperfine and quadrupole couplings of pyrrole nitrogen. *J. Phys. Chem.* **97**, 11858–11860 (1993).
79. H.-I. Lee, K. S. Thrasher, D. R. Dean, W. E. Newton, B. M. Hoffman, 14N electron spin−echo envelope modulation of the S = 3/2 spin system of the *Azotobacter vinelandii* nitrogenase iron−molybdenum cofactor. *Biochemistry* **37**, 13370–13378 (1998).
80. L. L. Yap, R. I. Samoilova, R. B. Gennis, S. A. Dikanov, Characterization of the exchangeable protons in the immediate vicinity of the semiquinone radical at the QH site of the cytochrome bo3 from *Escherichia coli*. *J. Biol. Chem.* **281**, 16879–16887 (2006).
81. S. A. Dikanov, A. M. Tyryshkin, I. Felli, E. J. Reijerse, J. Huttermann, C-band ESEEM of strongly coupled peptide nitrogens in reduced two-iron ferredoxin. *J. Magn. Reson. B* **108**, 99–102 (1995).
82. S. A. Dikanov, M. K. Bowman, Cross-peak lineshape of two-dimensional ESEEM spectra in disordered $S = 12$, $I = 12$ spin systems. *J. Magn. Reson. A* **116**, 125–128 (1995).
83. C. S. Burns, E. Aronoff-Spencer, C. M. Dunham, P. Lario, N. I. Avdievich, W. E. Antholine, M. M. Olmstead, A. Vrielink, G. J. Gerfen, J. Peisach, W. G. Scott, G. L. Millhauser, Molecular features of the copper binding sites in the octarepeat domain of the prion protein. *Biochemistry* **41**, 3991–4001 (2002).
84. S. A. Dikanov, M. K. Bowman, Determination of ligand conformation in reduced [2Fe-2S] ferredoxin from cysteine β-proton hyperfine couplings. *J. Biol. Inorg. Chem.* **3**, 18–29 (1998).
85. D. R. Kolling, R. I. Samoilova, A. A. Shubin, A. R. Crofts, S. A. Dikanov, Proton environment of reduced Rieske iron−sulfur cluster probed by two-dimensional ESEEM spectroscopy. *J. Chem. Phys. A* **113**, 653–667 (2009).

Acknowledgments: We thank G. C. Dismukes for providing access to the Bruker EPR Spectrometer. **Funding:** This work was supported by NASA Astrobiology Institute Grant "ENIGMA—Evolution of Nanomachines in Geospheres and Microbial Ancestors" (80NSSC18M0093) and the Gordon and Betty Moore Foundation on "Design and Construction of Life's Transistors" (GBMF-4742). (to V.N. and P.G.F.). S.P. was supported by the NASA Postdoctoral Program at the Astrobiology Institute, administered by Universities Space Research Association under contract with NASA. **Author contributions:** J.A.M., D.H.P., S.P., J.T., A.M.T., K.M.W., V.N., and P.G.F. designed the research; J.A.M., D.H.P., S.P., J.T., A.M.T., P.M.M., J.S., and J.J.M. performed the research; J.A.M., D.H.P., S.P., J.T., A.M.T., P.M.M., J.S., J.J.M., K.M.W., R.L.K., V.N., and P.G.F. analyzed the data; J.A.M., D.H.P., S.P., J.T., A.M.T., V.N., and P.G.F. wrote the paper. **Competing interests:** U.S. Patent Application No. 18/047,822, "A Minimal Catalytic D-Nickel Peptide Capable of Sustained Hydrogen Evolution and Methods of Use Thereof"—current status: pending—was submitted on 19 October 2022 by Rutgers, The State University of New Jersey. Authors also listed as inventors on the patent are as follows: J.A.M., D.H.P., S.P., J.T., A.M.T., V.N., and P.G.F. The authors declare that they have no other competing interests. **Data and materials availability:** All data needed to evaluate the conclusions in the paper are present in the paper and/or the Supplementary Materials. protCAD software and manual can be found on github.com/protCAD/protCAD and on Zenodo at DOI 10.5281/zenodo.7555626. AMBER molecular dynamics parameter files are available on Zenodo at DOI 10.5281/zenodo.7555782

Submitted 23 March 2022
Accepted 7 February 2023
Published 10 March 2023
10.1126/sciadv.abq1990

ScienceAdvances

Design of a minimal di-nickel hydrogenase peptide

Jennifer Timm, Douglas H. Pike, Joshua A. Mancini, Alexei M. Tyryshkin, Saroj Poudel, Jan A. Siess, Paul M. Molinaro, James J. McCann, Kate M. Waldie, Ronald L. Koder, Paul G. Falkowski, and Vikas Nanda

Sci. Adv., **9** (10), eabq1990.
DOI: 10.1126/sciadv.abq1990